ELSEVIER

Journal of Nuclear Materials 277 (2000) 91–98

journal of nuclear materials

www.elsevier.nl/locate/jnucmat

Texture of welded joints of 316L stainless steel, multi-scale orientation analysis of a weld metal deposit

G. Bouche[a,*], J.L. Béchade[b], M.H. Mathon[c], L. Allais[b], A.F. Gourgues[a], L. Nazé[a]

[a] *Ecole des Mines de Paris, Centre des Matériaux, UMR CNRS 7633, BP87 91003, Evry cedex, France*

[b] *Commissariat à l'Energie Atomique DTA/CEREM/DECM/Service de Recherches Métallurgiques Appliquées, Centre d'étude de Saclay 91191, Gif sur Yvette cedex, France*

[c] *Commissariat à l'Energie Atomique, DSM/Laboratoire Léon Brillouin, Centre d'étude de Saclay, 91191 Gif sur Yvette cedex, France*

Received 15 February 1999; accepted 4 June 1999

Abstract

Weld material of type 316L is widely used in stainless steel X weldments in fast breeder reactors. As it is difficult to cut test specimens from an X weldment, the two-phase microstructure of 316L welds was simulated by manually filling a mould with longitudinally deposited weld beads. The material consists of γ columnar grains which form a matrix where δ-ferrite dendrites can be found. The crystallographic texture of the material was investigated on the basis of a multi-scale approach. Neutron diffraction analysis showed that on a macroscopic scale both phases had predominantly the same fibre texture with some reinforcements, $\{1\,0\,0\}_\gamma$ being parallel to $\{1\,0\,0\}_\delta$. Further analysis on an increasingly fine scale were then carried out by EBSD and by TEM, showing that the ferrite dendrites were nearly parallel to the neighbouring austenite columnar grains

PACS: 87.64.Bx

1. Introduction

Weld material of type 316L was employed in making the welded joints of fast breeder reactors. Compositions of filler metals have been optimised in order to limit as far as possible the safety factor for the calculation of the strength of components with welds in the licensing procedure [1]. The microstructure of as-welded 316L weld deposit consists of two phases: columnar grains of γ-austenite constitute a matrix where thin dendrites of δ-ferrite can be found. The present paper deals with the texture of both phases. To minimise the interface energy involved, these two phases often present in steels misorientation relationships such as these described by Kurdjumov–Sachs (KS) or Nishiyama–Wassermann (NW). The texture resulting from the solidification process may induce an anisotropy in the creep behaviour which has been experimentally observed and reported elsewhere [2]. Actually, Greenwood [3] highlighted the role, with respect to creep, of the microstructural features and of anisotropy in the material. Metallographic observations performed on polished cross sections of creep tested samples show that creep damage is located at $\gamma-\gamma$ grain boundaries [2]. The purpose of this paper is to study the texture of the material in order to assess the influence of the crystallographic texture upon creep behaviour and localisation of damage initiation. The texture was studied at three different scales of the material making it a multi-scale data collection and interpretation. Global texture measurements were performed using neutron diffraction analysis. The results were complemented by more local orientation investigation using electron back-scatter diffraction (EBSD) and transmission electron microscopy (TEM). Those results are interpreted in terms of solidification mechanisms.

* Corresponding author.

E-mail addresses: bouche@mat.ensmp.fr (G. Bouche), mathon@bali.saclay.cea.fr (M.H. Mathon), allais@centre.saclay.cea.fr (L. Allais).

0022-3115/00/$ - see front matter
PII: S0022-3115(99)00134-8

2. Material: composition and processing

2.1. Composition

The filling metal used for the welded joints is a 316L type 19Cr–12Ni–2Mo stainless steel. The chemical composition of the material is given in Table 1. In this steel the amounts of nitrogen and molybdenum are controlled in order to improve creep resistance. The composition of the material is close to that of the fully austenitic base metal, except that the balance between γ and δ stabilising elements was chosen to result in 5–10% ferrite left in the weld. This was done to prevent hot liquidation during the solidification of the material [4]. This composition has proven as well to be beneficial for creep strength [5].

2.2. Weld metal preparation

The actual welded joints encountered in the elements of a typical nuclear power plant are X section weldments. Since it is difficult to cut test specimens from an X weldment, a piece of material was built using the manual filling metal arc technique. The analogue of the two-phase microstructure of 316L stainless steel welds was obtained by manually filling a mould with 82 longitudinal deposited weld beads. Welding current intensity was 140 A, with an electrode translation speed of approximately 25 cm/min. Fig. 1 schematically shows a transverse cross section of the mould where several deposited beads can be identified. Fig. 1 includes the conventional orientations for longitudinal (L), transverse (T) and short transverse (ST) directions and the location of the samples used for the various experiments reported in this paper.

2.3. Microstructure

Fig. 2 presents a scanning electron micrograph of the microstructure: the black phase is skeletal bcc ferrite while fcc austenite grains appear in grey. Bead deposition results in the formation of a complex two-phase (γ + δ) material in which γ is the dominant phase (94%). The γ phase is organised into columnar grains several millimetres long and approximately 50–100 μm across the section. Grains are oriented close to the ST direction by both the thermal solidification gradient and fluid mechanics in the weld-pool during solidification. As will be shown later, the consequence is a strong crystallographic texture. The second phase is residual δ-ferrite. The amount of δ, 6% ± 0.5%, has been experimentally measured using a magnetic gauge. The chemical composition should allow a fully austenitic material to be obtained at equilibrium. The presence of ferrite in the present case is due to the rapid solidification of the weld which is equivalent to a quench. Thin dendrites of ferrite, less than 1 μm thick, are observed within the austenite grains. The boundary between two austenite grains is also partially filled by δ-ferrite.

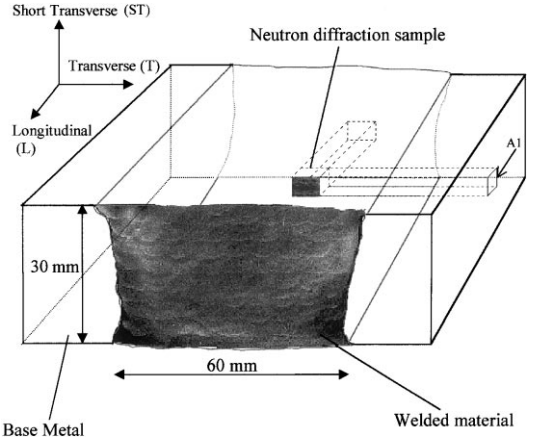

Fig. 1. Schematic sketch of the 316L mould and location of samples used in the present study.

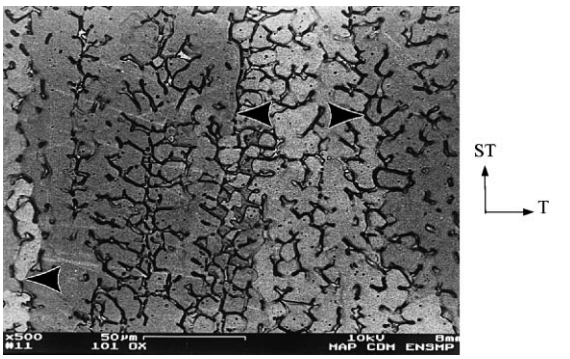

Fig. 2. Scanning electron micrograph of the microstructure showing both austenite and skeletal ferrite.

3. Procedure

3.1. Multi-scale approach

A volumic texture analysis was performed using the neutron diffraction technique. One of its specificities is to

Table 1
Chemical composition of the material used in the study (wt%)

C	Mn	Si	Cr	Ni	Mo	P	Ti	Nb	B	N	S
0.050	1.64	0.58	18.5	12.0	2.1	0.017	0.03	<0.05	0.0007	0.039	0.011

measure complete pole figures in transmission mode whereas conventional X-ray pole figures are disturbed for high tilt angles (χ). Other advantages are that no surface preparation is required for the sample and that the analysed volume can be up to 1 cm^3, which gives a very good statistics on texture for material with large grains as compared to small-scale investigations. In the case of the weld metal, γ grains can be as long as 1 cm in the direction of solidification. Furthermore, the neutron diffraction technique is very sensitive to small amount of second minor phase, here ferrite (<7 wt%).

EBSD was used to obtain crystallographic information from small regions of the bulk specimen, i.e. 30 nm in depth and up to 0.5 μm in diameter. This analysis was performed to investigate the crystallographic misorientation between the δ skeletal arms and the surrounding γ grains. The local texture data were compared with the data obtained by neutron diffraction on a macroscopic scale.

The crystallographic misorientation relationship between δ and γ was also investigated by selected area diffraction in TEM performed at the very close vicinity of the $\delta-\gamma$ interfaces.

3.2. Experimental procedure

3.2.1. Neutron diffraction

The experiments were performed at Laboratoire Léon Brillouin CEA, Saclay, on a four circle diffractometer, 6T1, dedicated to pole figure determination. The neutron wavelength was 1.159 Å, selected by a Cu (1 1 1) monochromator [6]. The sample was a cube of 0.6 cm edge. Its position and orientation in the mould are given in Fig. 1.

The scans were performed with steps of 5° and 3.75°, respectively, for χ and ϕ. The pole figures which were thus established were {1 1 1}, {2 0 0}, {2 2 0} and {3 1 1} for the austenitic phase, {1 1 0}, {2 0 0} and {2 1 1} for the ferritic phase. The Bragg angles of $\{1\,1\,1\}_\gamma$ and $\{1\,1\,0\}_\delta$ are so close to each other, that strong collimations had to be used to assess separately these pole figures. No absorption correction was applied.

Texture in polycrystalline materials is described quantitatively by the orientation distribution function (ODF) which is a three-dimensional function in Euler space (here Euler angles ψ, θ and φ, with the Roe notation) [7,8]. Every point $g_i(\psi, \theta, \varphi)$ represents a crystal orientation with respect to the specimen co-ordinate system, and the value of the function $f(g_i)$ is proportional to the volume fraction of crystals having an orientation $g_i + \Delta g$, Δg being a small orientation interval around g_i. In most cases, the function is printed out in table form, with the function values given for one variable constant and the other two variables with certain steps.

The ODF was calculated using the iterative series expansion method up to the rank $l_{max} = 22$, for even l only [9–11]. The pole figures were then recalculated from the ODF and compared with the experimental ones.

3.2.2. EBSD

An EBSD microstructural study was performed on a sample of the as-welded material. The surface analysed laid on the *T*–ST plane of the initial mould. The sample was mechanically polished up to a 1/4 μm grade and then electrolytically polished in a solution of 45% butoxyethanol, 45% acetic acid and 10% perchloric acid, at 4°C, 8 V for 8 s. A map was obtained on a 432 μm × 1 mm surface, with 4.5 μm steps between two measurements, in order to locate the $\gamma-\gamma$ high angle boundaries. The ferrite arms being so thin, the austenite alone was analysed in the map. Using this map, local orientation measurements were then carried out at the $\gamma-\gamma$ boundaries to investigate possible orientation relationships at a local scale between austenite and the thin ferrite skeleton lying in these boundaries. In addition, the δ/γ orientations were also investigated along the austenite low-angle boundaries.

EBSD measurements were carried out on a Zeiss DSM 982 Gemini high resolution SEM equipped with a Field Emission Gun and CCD low-light camera with on-ship integration. The SEM was operated at 20 kV with the sample tilted at 70°.

3.2.3. TEM

TEM investigations were performed on thin foils taken out from the bulk sample described in Section 2.2. Cores of 3 mm diameter were spark machined along the longitudinal directions of the weld beads. TEM samples were prepared by mechanically and electrochemically thinning slices of the cores. The thin foils then approximately lie on the *T*–ST plane of the bulk sample. The electrochemical thinning was performed by using the twin jet method in a 10% perchloric acid–45% acetic acid–45% butoxyethanol solution at 0°C with a 15 mA current in a Fischione electropolisher operating at 40 V. A groove marking the ST direction had been machined along the cores before slicing them. A notch thus appeared in each thin foil, which, by aligning it with the tilt axis of the goniometric stage of the TEM, allowed to approximately locate the ST direction in each studied area. TEM examinations were performed with a Philips EM430T microscope operating at a 300 kV accelerating voltage.

4. Experimental results

4.1. Neutron diffraction

The diffraction pattern presented in Fig. 3 shows the diffraction peaks related to both δ and γ phases. Next stage in the neutron diffraction analysis was to

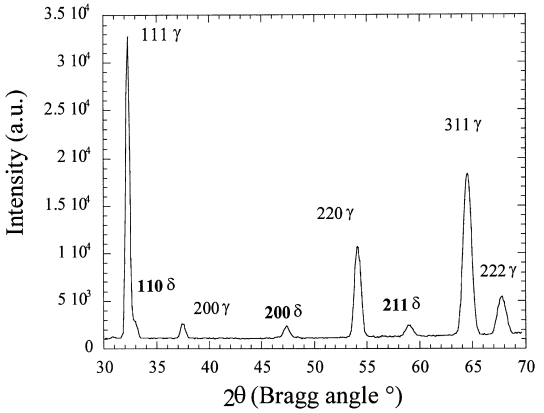

Fig. 3. Neutron diffraction pattern showing the two phases.

determine pole figures for the two phases. Experimental pole figures for each phase are presented in Figs. 4 and 5, respectively, {1 1 1}, {2 0 0}, {2 2 0} and {3 1 1} pole figures for γ and {1 1 0}, {2 0 0} and {2 1 1} pole figures for δ.

These pole figures are not in the plane of the A1 surface (Fig. 1) but have been tilted to have the growing direction of the grains perpendicular to the pole figure. This enabled to calculate the exact angular deviation α

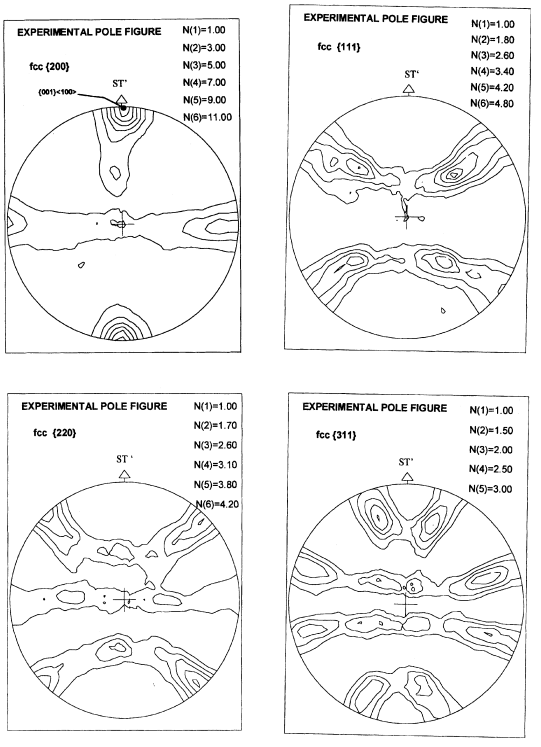

Fig. 4. Pole figures obtained for austenite by neutron diffraction analysis.

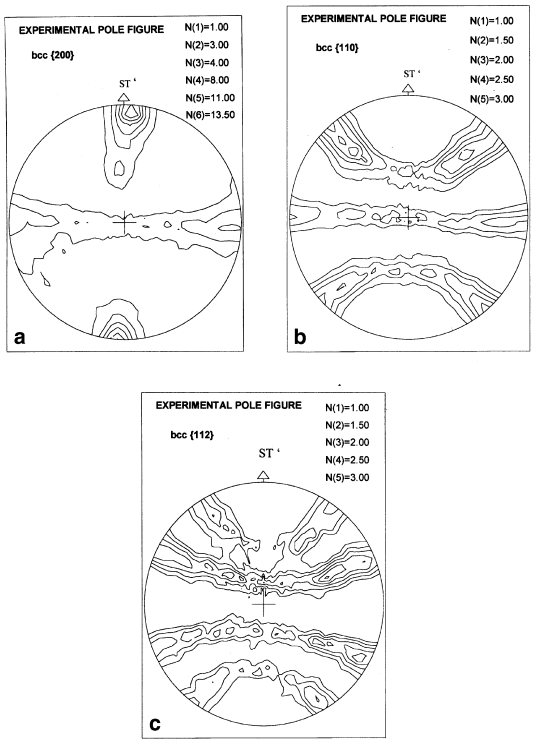

Fig. 5. Pole figures obtained for ferrite by neutron diffraction analysis.

between the ⟨1 0 0⟩ direction of solidification and the ST direction of the mould. The angle α can be divided, in the ST, T, L co-ordinate system of the mould, into a misorientation of $\beta = 20°$ on the ST–T plane and $\omega = 10°$ on the ST_β–L plane as presented in Fig. 6.

The figures obtained are the ones of a fibre-like ⟨1 0 0⟩ texture with reinforcements, and γ−δ pole figures are very similar. It clearly appears that the growing direction of the grains is of a type ⟨1 0 0⟩ parallel to ST′ (which is the transformation of ST after β and ω rotations).

The skeleton line, presented in Fig. 7, which gives the values of the ODF along a specifically chosen linear path through the orientation space (here for $\psi = 90$, $\varphi = 0$ and θ ranging from 0° to 180°), confirms the similarity between γ and δ pole figures. This plot also shows that the main orientation, {0 0 1}⟨1 0 0⟩, is a little bit stronger for the γ phase. As a consequence it comes out that on the macroscopic scale the phases are not in a classical orientation relationship like KS or NW but more in a cube–cube one.

4.2. EBSD-microstructure

The quite surprising crystallographic relationships between the δ and γ phases found by neutron diffraction

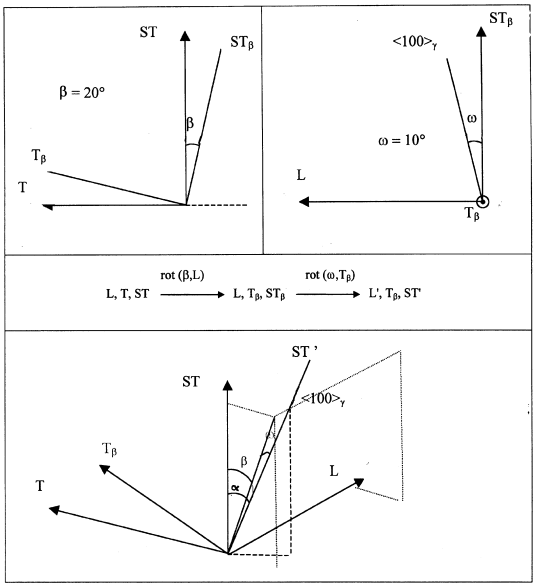

Fig. 6. Macroscopic angles of rotation between respectively the $\langle 1\,0\,0\rangle$ fibre for both γ and δ and the ST direction of the mould.

were assessed by EBSD studies on a local scale. Single point measurements were carried out, following both the high-angle and the low-angle γ grain boundaries. For each ferritic area encountered, the orientation of the two neighbouring γ grains was also determined close to δ. Figs. 8 (a) and (b) show the pole figures of the $\{2\,0\,0\}_\delta$ with respect to the austenite cube, for δ located, respectively, at the low angle and the high angle γ–γ boundaries. It clearly appears that the γ/δ relationships are not always described by the classical KS or NW relationships, and that for the δ located at the low angle boundaries most of them are very near (within a 10° scatter) a cube–cube orientation, whereas in the high angle boundaries more δ/γ misorientation relationships

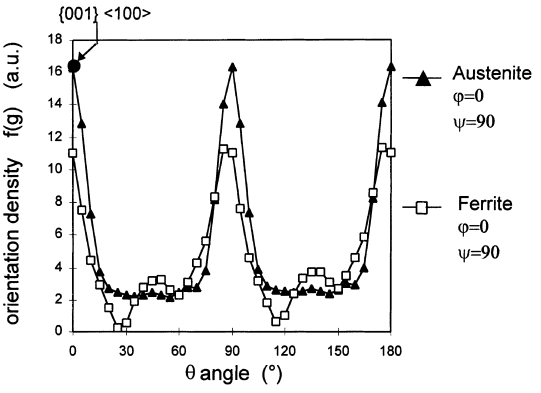

Fig. 7. Skeleton line of the ODF for $\varphi = 0$, $\psi = 90$ and θ ranging from 0° to 180°.

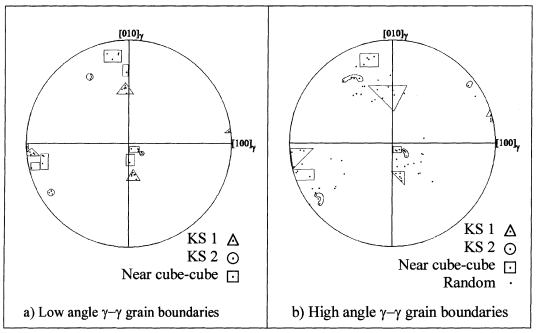

Fig. 8. EBSD results: (a) Pole figure for the low-angle grain boundary population of ferrite; (b) Pole figure for the high-angle grain boundary population of ferrite.

are described by the KS relationships, but only on one side of the δ grain. Thus, the non-classical results obtained by neutron analysis were confirmed by EBSD on a more local scale.

4.3. TEM

The observations by TEM confirmed the skeletal aspect of the ferrite embedded in the austenite matrix. As observed in the thin foil plane in Fig. 9, the ferrite arms were often thinner than 1/4 μm and seldom reached 1.5 μm thickness. The lattice built by the ferrite arms in an austenite grain presented loops of various widths, ranging from some μm to several tens μm. The austenite–ferrite boundaries were smoothly curved and planar interfaces were not very usual. The austenite presented a rather high and homogeneous dislocation density and the dislocation microstructure could not be characterised by any clear organisation feature. Dislocations in the ferrite were much more sparse and often arranged in pile-ups.

For each studied area of the foils, a stereographic projection of the ferrite arm and another one of the neighbouring austenite were built in the reference directions of the goniometric stage. The superimposition of these two stereographic projections gave the relative crystallographic orientation of the two phases.

In a number of cases, the $\langle 1\,0\,0\rangle$ directions of the ferrite and the austenite were slightly misoriented one from the other, with an angle that can reach 15° but the two phases could be believed to have grown according the $\langle 1\,0\,0\rangle_\delta // \langle 1\,0\,0\rangle_\gamma$ relative orientation. The misorientation did not seem to result from a relative rotation of the structures of the two phases around a dedicated crystallographic direction. Other areas presented a relative crystallographic orientation of the ferrite and its surrounding austenite for which only one $\langle 1\,0\,0\rangle$ direction could be considered to be common to both phases.

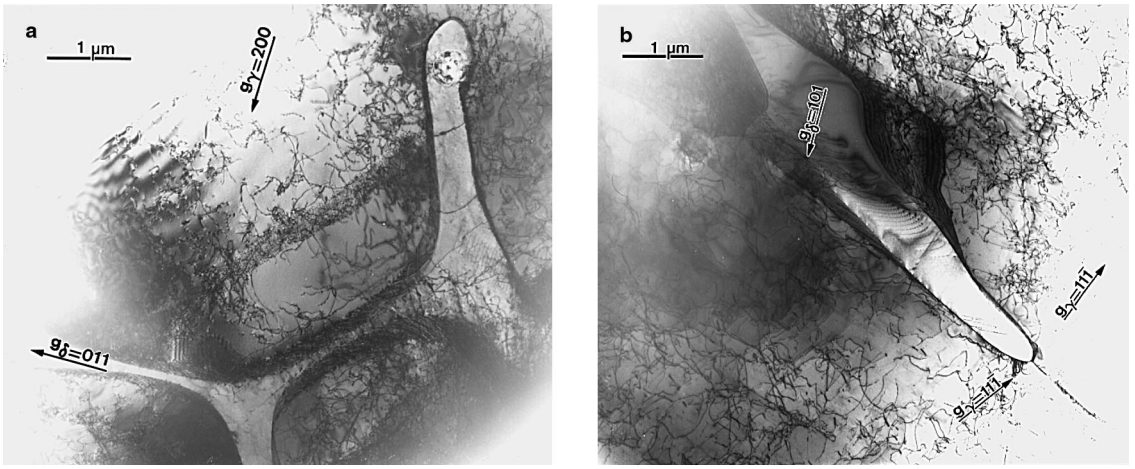

Fig. 9. TEM images of δ-ferrite in γ-austenite. The deviation from the cube–cube relative misorientation of the two phases allowed convenient two-beam conditions for imaging the dislocation microstructure in each pase: (a) Bright field image of intragranular δ-ferrite ($g_\delta = 0\,1\,1$) in γ-austenite ($g_\gamma = 2\,0\,0$); (b) Bright field image of intergranular δ-ferrite ($g_\delta = 1\,0\,1$) between two γ-austenite grains ($g_\gamma = 1\,1\,1$ in both grains). This δ-ferrite arm was not in a cube–cube relative misorientation with any of the two austenite grains.

In some cases the comparatively close correspondence of $[1\,0\,0]_\gamma$ and $[1\,0\,0]_\delta$ came with a reasonable respect of the relations $(1\,1\,0)_\delta // (1\,1\,1)_\gamma$ and $[-1\,1\,1]_\delta // [-101]_\gamma$ which place the two phases in a KS relative orientation.

Though no statistical distribution of specific orientations such as cube–cube orientation or KS orientation can be deduced from 20 or so orientation analyses, the cube–cube orientation seemed to be prevailing for intergranular δ-ferrite, when the KS orientation were not often encountered.

Again within the limit we may give to the statistical representativeness of such a study, the possibly single common $\langle 1\,0\,0\rangle$ direction of the δ and γ appears to systematically be close to the ST′ direction.

5. Discussion

The fibre-like figure obtained for the austenitic matrix is in good agreement with the description of the microstructure of the material given in Section 2.3. The misorientation relationships between δ and γ phases are now discussed.

5.1. Multi-scale approach

A fibre-like texture as the one identified in the present study confirms the results of Takalo et al. [12] on a similar weld alloy. These authors present X-ray texture determinations on austenite but the texture of δ-ferrite could not be identified due to its low volume fraction. Although the material of the present study contains more ferrite, the success in acquiring pole figures for ferrite was essentially due to the specificity of neutron diffraction compared to X-ray diffraction, as discussed previously. Furthermore, there is no degradation of the signal as the χ tilt angle of the sample approaches 75° as it is the case for X-ray diffraction: the pole figure is consequently complete and the ODF more reliable. We have not been able to find results on such a neutron diffraction work on a bcc ferrite phase in the case of welded joint in the literature.

The ferrite shows a fibre-like texture with reinforcements. The pole figures of both phases are very similar and on a global scale, the ferrite and austenite phases were found not to maintain a KS misorientation relationship. Suutala et al. [13] reported a KS misorientation relationship between austenite and a lathy ferrite for a close in composition material by using TEM analysis only. Present EBSD and TEM studies show that the same conclusions as the ones obtained by neutron diffraction can be drawn on a microscopic scale, thus giving meaningful information about the solidification mechanisms acting during the welding process.

5.2. Solidification mechanisms on a macroscopic scale

Previous work by Finlan et al. [14] showed that the solidification mechanism of such stainless steel welds is complex, involving either primary ferrite solidification, or primary austenite solidification, or a simultaneous formation of δ and γ. The present results show that both δ and γ phases bear one common $\langle 1\,0\,0\rangle$ direction which can be thought as the solidification direction.

The misorientation between this $\langle 1\,0\,0\rangle_{\gamma,\delta}$ solidification direction and the ST direction is related to the making of the bulk sample: the ω angle (Fig. 6) results

from the combined effects of thermal gradient and fluid mechanics in the weld pool along with the inclination angle of the electrode during the process which made the solidification direction close to the vertical one in Fig. 1. The β angle is due to the multi-pass process used to fill the mould. A new bead laid upon two previous beads, one beneath and another one on its left which make the general orientation of the solidification direction slightly unbalanced on its right side. A single bead deposited on a plate would show a $\beta = 0$ angle.

5.3. Solidification mechanisms on a microscopic scale (EBSD/TEM)

Both EBSD and TEM give complementary results about the solidification mechanism. The ferritic phase found along the γ/γ low-angle boundaries generally shares the same orientation – very slight misorientation – with the neighbouring γ grains. It was partly the case for the high-angle boundary δ phase, being parallel to one of the neighbouring γ grains and more randomly oriented with respect to the other. The slight misorientation measured between γ and δ may result from reorganisations of the coexisting phases upon cooling, due to discrepancies in their thermal contraction. This supports the prevailing hypothesis of a parallel growth of the two phases. Another hypothesis would consist in considering a solid transformation $\delta \rightarrow \gamma$ or $\gamma \rightarrow \delta$. Actually, such a transformation would rather lead to straight boundaries and near KS misorientation relationships when it can be observed in Fig. 9 that $\gamma - \delta$ boundaries are curved.

More generally, the thermal stresses brought into action during the whole welding process induce rotations and plastic deformation of each phase which could explain both the relative misorientations of the two structures and the dislocation microstructures observed by TEM (Fig. 9).

The case of the high-angle boundary ferrite is complex, as the misorientation between the δ and the highly misoriented neighbouring γ grain seems to be random. The KS like relationships found in some cases do not prove that one of the two phases formed from the other, the frequency of their occurrence being not statistically significant. Actually these relationships are directly linked to the misorientation of the γ grains lying on both sides of the high-angle boundaries. This point is still under investigation, as no explanation has been found to account for the reinforcements observed on two directions perpendicular to the solidification direction (Figs. 4 and 5). Why the solidification gives birth to grains organised in such a way is still a problem to investigate. Nevertheless, the crystallographic anisotropy evidenced in this study plays a significant role in the mechanical properties of the material. With the data collected on the texture of the material, the anisotropy observed in its mechanical behaviour can be addressed. This aspect of the microstructure of stainless steel welds is to be studied in further work.

6. Conclusion

1. Texture for austenite is fibre texture with reinforcements perpendicular to the $\langle 0\,0\,1 \rangle_\gamma$ growing direction.
2. Complete pole figures for the minor (<7 wt.%) ferritic phase could be obtained with neutron diffraction analysis thus allowing a quantitative texture study of that phase.
3. The pole figures obtained for ferrite are very similar to the ones obtained for austenite, showing that δ and γ are mainly in a cube–cube misorientation relationship.
4. The same conclusion can be drawn from the EBSD and TEM studies on a local scale.
5. This has been interpreted in terms of the solidification mechanism: both ferrite and austenite cubes mostly nucleate and grow in parallel; then, upon cooling, plasticity occurred to accommodate the difference in the thermal expansion coefficients of both phases. This plasticity led to a misorientation (of up to 15°) between both phases.

Acknowledgements

The authors want to express their gratitude to Dr F. Grillon for his advise concerning STEM and EBSD analysis, to Professor A. Pineau and Professor R. Piques for their valuable comments, and to CEA/CEREM and CEA/IPSN for their financial support.

References

[1] E. Ohrt, E. te Heesen, Nucl. Eng. Design 130 (1991) 1.
[2] G. Bouche, L. Allais, V. Lezaud, R. Piques, A. Pineau, Mater. High Temp. 15 (3/4) (1998) 403.
[3] G.W. Greenwood, An overview of failure mechanisms in creep, in: Proceedings of the 12th European Conference on Fracture: Fracture from defects, 1998, pp. 3–14.
[4] J.A. Brooks, A.W. Thompson, Int. Mater. Rev. 36 (1) (1991) 16.
[5] R.G. Thomas, Welding J. Res. Suppl. (1978) 81s.
[6] L.L.B.: Laboratoire Léon Brillouin, Equipements expérimentaux, CEA Saclay, 1995, pp. 41–42.
[7] R.J. Roe, J. Appl. Phys. 36 (1965) 2024.
[8] R.J. Roe, J. Appl. Phys. 37 (1966) 2069.
[9] A.S. Viglin, Sov. Phys. Solid State 2 (1960) 2195.
[10] H.J. Bunge, Z. Metalllkd. 56 (1965) 827.
[11] H.J. Bunge, Texture Analysis in Material Science, Butterworths, London, 1982.

[12] T. Takalo, N. Suutala, T. Moisio, Metall. Trans. 10A (1979) 1173.
[13] N. Suutala, T. Takalo, T. Moisio, Metall. Trans. 10A (1979) 1183.
[14] G.T. Finlan, Y.P. Lin, J.W. Steeds, in: Materials for Nuclear Core Applications, BNES, London, 1987, p. 147.